Composite Hydrogels with Tunable Anisotropic Morphologies and Mechanical Properties

Mokit Chau[‡], Kevin J. De France[‡], Bernd Kopera, Vanessa R. Machado, Sabine Rosenfeldt, Laura Reyes, Katelyn J. W. Chan, Stephan Förster, Emily D. Cranston, Todd Hoare, Eugenia Kumacheva

DOI: **10.1021/acs.chemmater.6b00792**

Composite Hydrogels with Tunable Anisotropic Morphologies and Mechanical Properties

Mokit Chau[1‡], Kevin J. De France[2‡], Bernd Kopera[1,3], Vanessa R. Machado[1], Sabine Rosenfeldt[3], Laura Reyes[1], Katelyn J. W. Chan[2], Stephan Förster[3], Emily D. Cranston[2]*, Todd Hoare[2,4]*, Eugenia Kumacheva[1,5,6]*

[1] Department of Chemistry, University of Toronto, 80 Saint George Street, Toronto, Ontario M5S 3H6, Canada

[2] Department of Chemical Engineering, McMaster University, 1280 Main Street West, Hamilton, Ontario L8S 4L7, Canada

[3] Physical Chemistry I, University of Bayreuth, 30 Universitätsstraße, Bayreuth, DE 95440, Germany

[4] School of Biomedical Engineering, McMaster University, 1280 Main St. West, Hamilton, Ontario

L8S 4L7, Canada

[5] Department of Chemical Engineering and Applied Chemistry, University of Toronto, 200 College Street, Toronto, Ontario M5S 3E5, Canada

[6] The Institute of Biomaterials and Biomedical Engineering, University of Toronto, 4 Taddle Creek Road, Toronto, Ontario M5S 3G9, Canada

[†] Authors contributed equally

KEYWORDS hydrogels, cellulose nanocrystals, freeze-cast, freeze cast, ice-template, anisotropic, cryogel, aerogel, xerogel

ABSTRACT: Fabrication of anisotropic hydrogels exhibiting direction-dependent structure and properties have attracted great interest in biomimicking, tissue engineering and bioseparation. Herein, we report a single-step freeze casting-based fabrication of structurally and mechanically anisotropic aerogels and hydrogels composed of hydrazone cross-linked poly(oligoethylene glycol methacrylate) (POEGMA) and cellulose nanocrystals (CNCs). We show that by controlling the composition of the CNC/POEGMA dispersion and the freeze casting temperature, aerogels with fibrillar, columnar, or lamellar morphologies can be produced. Small-angle X-ray scattering experiments show that the anisotropy of the structure originates from the alignment of the mesostructures, rather than the CNC building blocks. The composite hydrogels show high structural and mechanical integrity and a strong variation in Young's moduli in orthogonal directions. The controllable morphology and hydrogel anisotropy, coupled with hydrazone cross-linking and biocompatibility of CNCs and POEGMA, provide a versatile platform for the preparation of anisotropic hydrogels.

INTRODUCTION

Hydrogels have a broad range of applications in drug delivery,[1] tissue engineering,[2,3] separation of biological molecules,[4] and water purification.[5] The utilization of hydrogels as biomaterials has a particular appeal, since they can be engineered to exhibit biophysical and chemical properties that are similar to native extracellular matrix. Since many tissues, e.g., striated muscle,[6] cartilage,[7] or cornea[8], to name just a few examples, have anisotropic hierarchical morphologies, there is a growing interest in developing approaches for the fabrication of anisotropic hydrogels that exhibit direction-dependent pore shape, microstructure, stiffness, and conductivity.[6–21] In tissue engineering, aside from biomimicry, anisotropic pore shape and hydrogel structure, in general, are important for cell guidance[22] and differentiation,[23] as well as mass transport of biofactors and nutrients throughout the scaffold.[19,24,25] In bioseparation, control over the shape anisotropy of hydrogel pores may enhance the selectivity of the filtration of biological species and/or minimize the pressure drop across the matrix.[26]

Anisotropic hydrogels have been fabricated by applying tensile or compressive forces to shape-anisotropic gel components, e. g., carbon nanotubes or cellulose nanocrystals, within an isotropic hydrogel matrix.[13,15,27,28] Self-assembled fibrils of peptide amphiphiles[26] or lamellar bilayers of polymerizable surfactants[25, 27] have been oriented within a hydrogel matrix using shear forces. Alternately, dielectrophoresis has been utilized to align carbon nanotubes in an isotropic hydrogel matrix.[17] Micropatterning approaches [7] and 3D printing[31] have been applied to create anisotropic hydrogels with pores of well-defined sizes and geometries.

Directional freeze-casting (also known as ice-templating) is another promising method for fabricating anisotropic gels with a well-defined porous structure.[19,20,24,25,32–36] In this method, precursor solutions or suspensions of monomers or polymers are frozen under a unidirectional temperature gradient, thereby excluding the solute from the ice lattice into the space between the growing ice crystals.[37–39] To form a hydrogel, the resulting free-standing microporous scaffold is swollen with water. The elongated pore shapes in the hydrogel replicate the shapes of the unidirectionally grown ice crystals.

Generally, in order to prevent re-dissolution of the freeze-cast scaffold upon its immersion in water, post-processing material photocrosslinking or photopolymerization are used.[18,20,26,32,40–42] A more efficient strategy would be simultaneous freeze-casting and cross-linking, as demonstrated for anisotropic hydrogels of agarose[34] and glutaraldehyde-crosslinked gelatin[43]. This alternative approach can be readily implemented in composite hydrogels, in addition, to greater morphological control achieved by varying the ratio of hydrogel components.

Recently, cellulose nanocrystals (CNCs) have gained interest as a component of composite hydrogels, due to the mechanical strength, commercial availability, and biocompatibility of CNCs.[44] Cellulose nanocrystals have been used as reinforcing agents for isotropic hydrogels.[45–53] Hydrogels have been prepared from freeze-cast suspensions of CNCs and xylan, in which the xylan component modified with aldehyde groups formed hemiacetal bonds with the xylan.[35] In these hydrogels, however the fast hydrolysis of hemiacetals may limit the stability of the resulting material.[54]

Here, we report the fabrication of anisotropic CNC-containing hydrogels that have two novel and advantageous features: (i) they are derived from precursor aerogels prepared *via* a single-step freeze-casting and cross-linking process, and (ii) they are cross-linked *via* more stable, slowly hydrolyzable bonds, which is critical in the context of tissue engineering. Importantly, we show the ability to generate precursor aerogels with fibrillar, columnar and lamellar morphologies, leading to direction-dependent swelling and mechanical properties of the resulting hydrogels.

We used aldehyde-functionalized CNCs and hydrazide-functionalized poly(oligo ethylene glycol methacrylate) (POEGMA) as aerogel components. Hydrazone bonds formed between aldehyde and hydrazide groups are hydrolytically degradable, relatively slowly (over months) at neutral pH but significantly faster at acidic pH values.[55] The microstructure of the aerogels and the resulting hydrogels was controlled by varying the weight ratio of CNC-to-POEGMA, the total concentration of these components in the precursor suspension, and the freeze-casting temperature. The well-established cytocompatibility of CNCs[44,56–58] and POEGMA,[59,60] the degradability of the hydrazone cross-linked networks, and the anisotropy of these hydrogels suggests their potential utility in biomedical applications.

EXPERIMENTAL SECTION

Materials. Oligo(ethylene glycol) methyl ether methacrylate (OEGMA500, Sigma Aldrich, 95%) and di(ethylene glycol) methyl ether methacrylate (M(EO)2MA, Sigma Aldrich, 95%) were purified using a column of basic aluminum oxide (Sigma Aldrich, type CG-20). Acrylic acid (AA, Sigma Aldrich, 99%), 2,2-azobisisobutyric acid dimethyl ester (AIBMe, Wako Chemicals, 98.5%), adipic acid dihydrazide (ADH, Alfa Aesar, 98%), *N*'-ethyl-*N*-(3-dimethylaminopropyl)-carbodiimide (EDC, Carbosynth, Compton CA, commercial grade), thioglycolic acid (TGA, Sigma Aldrich, 98%), sodium periodate ($NaIO_4$, Sigma Aldrich, >99.8%), sodium hydroxide (EMD Millipore Germany), sodium chloride (Sigma Aldrich, ≥99.5%), hydrochloric acid (LabChem Inc., 1M), silver(I) oxide (Sigma Aldrich, ≥99.99% trace metals basis), dioxane (Caledon Laboratory Chemicals, reagent grade) and sulfuric acid (Sigma Aldrich, 95-98%) were used as received. Whatman cotton ashless filter aid was purchased from GE Healthcare Canada. In all the syntheses and fabrication protocols Milli-Q grade distilled deionized water (DIW, 18.2 MΩ cm resistivity) was used.

Synthesis of hydrazide-functionalized poly (oligoethylene glycol methacrylate) (H-POEGMA). The synthesis of **H-POEGMA** is described elsewhere.[55,60] Briefly, AIBMe (74 mg), M(EO)2MA (6.2 g), OEGMA500 (1.8 g), AA (1046 µL) and TGA (150 µL, 10 w/w% in dioxane) were introduced into a round-bottom flask. Following the addition of dioxane (20 mL) to this mixture, it was purged with nitrogen for 30 min. The reaction proceeded for 4 h in an oil bath at 75°C, after which the solvent was removed *via* rotary evaporation. Following this step, 200 mL of deionized water was added to the resulting POEGMA solution along with ADH (8.66 g). To adjust the mixture pH to 4.75 ± 0.1, 1M HCl was used, after which EDC (3.87 g) was added to mediate conversion of carboxylic acid groups to hydrazide groups. The value of pH was maintained at 4.75 ± 0.1 *via* a dropwise addition of 1M HCl over 4 h, until no further pH change was noted, after which the reaction was allowed to proceed overnight. The product was dialyzed (molecular weight cutoff of 3,500 g mol^{-1}) against deionized water for a minimum of six 6 h cycles and then lyophilized. Polymers were stored as a 10 wt% suspension in deionized water at 4°C.

Hydrazide content (1.61 mmol/g hydrazide groups) was determined *via* conductometric titration (ManTech, 0.1 M NaOH titrant). The molecular weight of H-POEGMA of M_n = 17.7 kDa and polydispersity of 3.2 were determined by aqueous size exclusion chromatography on a Waters 515 HPLC pump with three Ultrahydrogel columns (30 cm x 7.8 mm i.d. with exclusion limits of 0–3 kDa, 0–50 kDa and 2–300 kDa) and a Waters 2414 refractive index detector. A mobile phase containing 25 mM *N*-cyclohexyl-2-aminoethanesulfonic acid (CHES) buffer, 500 mM $NaNO_3$ and 10 mM NaN_3 was used at a flow rate of 0.8 mL min^{-1}. The mole ratio of hydrazide-functionalized AA: M(EO)2MA:OEGMA500 was 0.28:0.64:0.061.

Preparation of cellulose nanocrystals. Cellulose nanocrystals were generated using the sulfuric acid-mediated hydrolysis of cotton.[61] Briefly, blended cotton filter aid was exposed to 64 wt% sulfuric acid solution at 45 °C for 45 min with mechanical stirring, diluted 10-fold in deionized water, and centrifuged for 10 min at ~5000 *g*. The acidic supernatant was decanted from the centrifuge tubes, leaving a cellulose pellet, since the CNCs were insoluble at acidic pH. The cycles of water adding, centrifuging, and decanting were repeated until a pellet no longer formed upon the addition of water. The resulting suspension was subsequently dialyzed (molecular weight cutoff 12-14,000 g mol^{-1}) against deionized water for a minimum of ten cycles of at least, 12 h each. The CNC suspension was then sonicated using a probe sonicator (Sonifier 450, Branson Ultrasonics, Danbury, CT) for three 15 min-long cycles and stored at 4 °C as a 1 wt% suspension in acid form (pH = 3.2). Sulfate half-ester content was determined by conductometric titration,[62] yielding a sulfur content of 0.42 wt % (~ 0.30 charges/nm^2). The CNC apparent diameter of 71 nm and electrophoretic mobility of -1.86 × 10^{-8} m^2 V^{-1} s^{-1} were determined by dynamic light scattering and electrokinetic potential measurements using a 0.25 wt % CNC suspension in 10 mM NaCl solution (Zetasizer Nano, Malvern, UK).

Preparation of aldehyde-functionalized cellulose nanocrystals (A-CNCs). The selective oxidation of CNC surface hydroxyl groups to aldehyde groups was optimized as described elsewhere.[63] Sodium periodate and a 1.0 wt% suspension of CNCs were added to a round-bottom flask at the $NaIO_4$:CNC weight ratio of 4:1. The flask was covered with aluminum foil to prevent $NaIO_4$ photo-decomposition. The pH value of the suspension was then adjusted to 3.5 and the suspension was placed under magnetic stirring in an oil bath at 45 °C for 4 h. The reaction was subsequently quenched by cooling the reaction mixture and exposing it to light to de-activate residual $NaIO_4$. The resulting product was dialyzed (molecular weight cutoff 12-14,000 g mol^{-1}) against deionized water for a minimum of ten cycles of at least, 12 h each. The suspension was concentrated to 8 wt% by ambient evaporation and stored at 4 °C. Aldehyde content of 3.66 mmol/g was determined by conductometric titration (ManTech, 0.1 M NaOH titrant) after selectively oxidizing aldehyde groups to carboxylic acids using silver(I) oxide, as described previously.[48] Atomic force microscopy was used to determine A-CNC dimensions to be 60-220 nm in length and 2-10 nm in diameter (Figure S1).

Preparation of anisotropic aerogels and hydrogels by freeze-casting. Two different assemblies were used for freeze-casting. Assembly 1 consisted of an aluminum block equilibrated in a Dewar filled with liquid nitrogen, enabling freeze-casting at a -196 °C. Assembly 2 consisted of a proportional-integral-derivative controlled heater assembly with a copper block on an aluminum rod, which enabled control over the freeze-casting temperature between -80 and -20 °C. An aqueous mixture of A-CNCs and H-POEGMA was charged into a tube closed on one end with a 0.9 mm-thick copper lid. Aerogels for SEM imaging and photographing were fabricated in a 1.3 cm inner diameter Teflon tube. Aerogels for compression tests and swelling experiments were fabricated in a polycarbonate cuboidal tube with the inner length and width of 0.95 cm. The filled mold was placed atop the cooled aluminum block (Assembly 1) or atop the cooled copper block (Assembly 2). Freezing was assessed visually. After that, the samples were maintained on the cooling block for an additional minute to ensure complete freezing and subsequently, freeze-dried in lyophilizer. To form hydrogels, freeze-casted aerogels were swollen in water.

Scanning electron microscopy. The resulting A-CNC-H-POEGMA aerogels were freeze-fractured either parallel, or perpendicular to the direction of freeze-casting, sputter-coated with gold, and imaged using a scanning electron microscope (SEM, Quanta FEI 250 scanning electron microscope, 10 kV).

Surface area determination. The surface area of aerogels was determined by volumetric nitrogen adsorption at 77 K using a Quantachrome Autosorb-1-C and calculated using a Brunauer-Emmet-Teller(BET) equation.[64] Aerogels were outgassed overnight at 80 °C (at 100°C the samples discoloured, possibly due to the polymer degradation).

Small-angle X-ray scattering. The aerogels were characterized at room temperature using a small-angle X-ray system (Double Ganesha AIR, SAXSLAB, Denmark). The X-ray source was a rotating anode (copper, MicoMax 007HF, Rigaku Corporation, Japan) that provided a micro-focused beam. The data were recorded by a position-sensitive detector (PILATUS 300K, Dectris). To cover the range of scattering vectors between 0.004-2.0 $Å^{-1}$ different detector positions were used. The circularly averaged data were normalized to incident beam intensity, sample thickness, and measurement time before subtracting the background (air). The data analysis was performed with the software Scatter (version 2.5), which was also used to perform calculations based on simple geometric models.[65] The irradiation volume was approximately 200 µm x 200 µm x 1 cm, where 1 cm is the sample thickness.

Hydrogel swelling. To characterize the anisotropic swelling of the hydrogels in deionized water, we defined a coordinate system for the cuboidal aerogel/hydrogel samples, in which the X- and Y-axes were orthogonal to the direction of ice growth., and the Z-axis was parallel to the direction of ice growth. The original cuboid aerogels had an equal length, l_o, and height, h_o. Upon swelling, at time t, the hydrogels acquired the corresponding dimensions, $l(t)$ and $h(t)$. The dimensions of aerogels and hydrogels were measured using a caliper at different time intervals. The degree of swelling in the XY-plane was determined as

$$Q_{XY}(t) = \frac{l(t)-l_o}{l_o} \quad (1)$$

The degree of hydrogel swelling in the Z-direction was characterized as

$$Q_z(t) = \frac{h(t)-h_o}{h_o} \quad (2)$$

Mechanical testing. Cyclic compression measurements were conducted in an aqueous environment at 22 °C using a Mach-1 Mechanical Tester (Biomomentum Inc, QC) operating under parallel-plate geometry. Prior to testing, aerogels with a width and length of 9.5 mm and a height of 11 to 14 mm were immersed in water for 10 min. The resulting hydrogels were compressed in either the XY-direction (perpendicular to the direction of freeze-casting) or the Z-direction (parallel to the direction of freeze-casting) over 50 cycles, by applying XY-strains of 50% or Z-strains of 10% (the samples buckled at Z-strains exceeding 10%). The tests were performed in triplicate, with the Young's modulus values calculated from the first compression cycle (after an initial pre-compression/pre-loading step to condition the hydrogels).

RESULTS AND DISCUSSION

Microstructure of anisotropic aerogels. H-POEGMA and A-CNCs were mixed and immediately freeze-cast in either cylindrical or cuboidal molds (Scheme 1). The final hydrogels were held together by physical crosslinks *via* non-covalent, hydrophobic interactions between H-POEGMA and A-CNCs, in addition to the covalent hydrazone cross-linking.[53] The aerogel structure and hydrogel mechanical properties were examined as a function of the weight ratio of A-CNC-to-H-POEGMA and the total concentration of A-CNCs and H-POEGMA in the mixture used for freeze-casting (this concentration was denoted as $C_{A\text{-}CNC+H\text{-}POEGMA}$).

Table 1 shows the recipes used for the preparation of the aero gels. Sample names are denoted as a:b-W@T, where a:b is the weight ratio of A-CNC-to-H-POEGMA, W is the $C_{A\text{-}CNC+H\text{-}POEGMA}$, and T is the temperature of freeze-casting. When no temperature T is specified in the sample notation, the freeze-casting process was conducted at -196 °C.

Scheme 1. Cross-linking reaction of aldehyde-modified CNCs (A-CNCs) with hydrazide-functionalized POEGMA (H-POEGMA) and illustration of morphologies of hydrogels achieved via the freeze-casting process

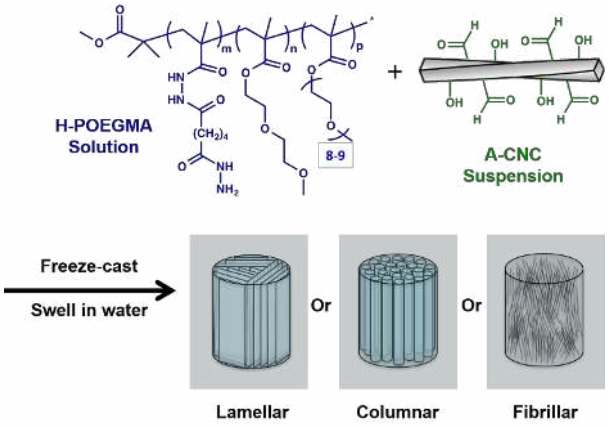

Table 1. Recipes of freeze-cast aerogels and hydrogels and Young's moduli of the rehydrated hydrogels

Sample name* (a:b-W@T)	Weight ratio of A-CNC:H-POEGMA	$C_{A\text{-}CNC+H\text{-}POEGMA}$ (wt%)	Freeze-cast temperature (°C)
1:1-4	1:1	4.0	-196
1:3-4	1:3	4.0	-196
1:5-4	1:5	4.0	-196
1:5-2.5	1:5	2.5	-196
1:5-7	1:5	7.0	-196
1:5-4 @-80	1:5	4.0	-80
1:5-4 @-20	1:5	4.0	-20

* When no temperature T is specified in sample name, the freeze-casting process was conducted at -196 °C.

** Calculated from the linear portion of the first stress-strain cycle applied.

Figure 1a shows SEM images of the cross-section of the aerogels in the XY-plane perpendicular to the ice-growth direction. Three general trends are evident from this figure. First, at the low $C_{A\text{-}CNC+H\text{-}POEGMA}$ and high weight fraction of A-CNCs in the precursor suspension, the aerogels had a fibrillar structure with fiber width of ~0.5 μm (top left image in Figure 1a). Second, the fibrillar structure transformed into a columnar structure when the $C_{A\text{-}CNC+H\text{-}POEGMA}$ was increased 4-7-fold at high A-CNC content (Figure 1a, top row, two right images). The pores had the width of ~4 μm and a wall thickness of ~100 nm. Third, at a high $C_{A\text{-}CNC+H\text{-}POEGMA}$ and a low weight fraction of A-CNCs, the aerogels had a lamellar morphology (Figure 1a, right column, two bottom images). The lamellae were ~200 nm-thick and an inter-lamellar distance was ~7 μm. The fibrillar, columnar, and lamellar structures are labeled as "F", "C" and "L", respectively, in the SEM images in Figure 1a. In the intermediate range of sample compositions, the aerogel morphologies were less defined and showed a transition from fibrillar-like to lamellar-like structures.

The ability of the free-standing aerogels to maintain the shape of the mold, that is, their structural integrity upon lyophilization, was examined with respect to both $C_{A\text{-}CNC+H\text{-}POEGMA}$ and the A-CNC-to-H-POEGMA weight ratio (Figure 1b). Although all samples did not disintegrate upon lyophilization, the greatest structural stability was observed for the aerogels with the $C_{A\text{-}CNC+H\text{-}POEGMA}$ of 2.5 and 7.0 wt%. Aerogels formed at lower $C_{A\text{-}CNC+H\text{-}POEGMA}$ did not contain a sufficient amount of material to preserve the aerogel shape. At high A-CNC fraction, the dimensional stability of aerogels after lyophilization improved, which was attributed to the mechanical strength of A-CNCs.

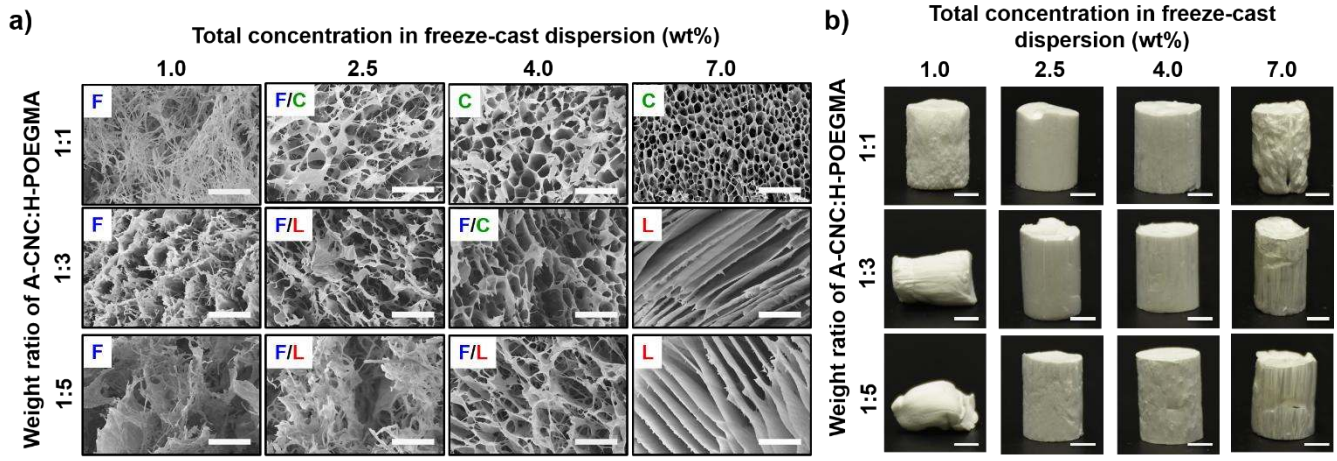

Figure 1. (a) SEM images of aerogels cross-section (the XY-plane perpendicular to the ice-growth direction) with morphologies ranging from fibrillar (F) to columnar (C) to lamellar (L) and their combinations, dependent on A-CNC:H-POEGMA weight ratio and $C_{A\text{-}CNC+H\text{-}POEGMA}$. Scale bars are 20 µm. (b) Photographs of aerogels cast in cylindrical molds. Scale bars are 0.5 cm.

In addition to varying aerogel composition, the freeze-cast temperature and thus the rate of ice crystal growth in the samples was used to control aerogel morphology (Figure 2). The aerogel freeze-cast at -20 °C formed a more well-defined lamellar-like structure, in comparison with the same sample prepared at -80 °C. At lower freezing velocities achieved at smaller temperature gradients, A-CNCs and H-POEGMA had sufficient time to be excluded from the growing ice crystals, thus yielding more organized structures.

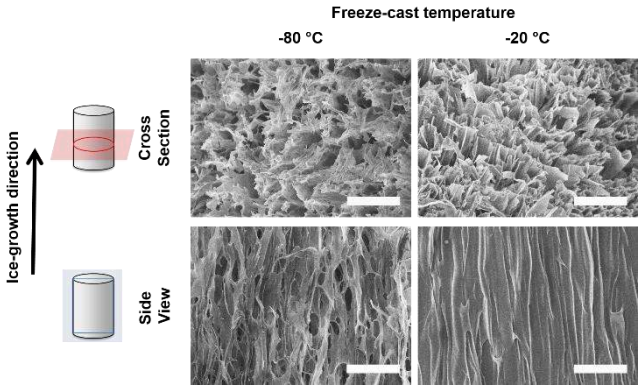

Figure 2. SEM images of aerogel 1:5-4 directionally freeze-cast from A-CNC + H-POEGMA dispersions at various temperatures. Top and bottom rows of images show the structure of the freeze-fractured planes that are perpendicular (cross-section) and parallel (side view), respectively, to the ice-growth direction, as shown in the corresponding cartoons. Scale bars are 50 µm.

Examination of the surface area of aerogels. The diverse morphologies of the aerogels were reflected by changes in their surface area (Figure 3a). At $C_{A\text{-}CNC+H\text{-}POEGMA}$ = 4.0 wt%, with increasing the A-CNC:H-POEGMA ratio the aerogel surface area increased from 18 (sample 1:1-4) to 33 m^2/g (sample 1:5-4), concurrent with the observed change in microstructure from columnar to sheet-like, respectively (Figure 1a). In contrast, at a constant A-CNC:H-POEGMA ratio of 1:5, increasing the $C_{A\text{-}CNC+H\text{-}POEGMA}$ from 4.0 to 7.0 wt% resulted in the decrease of the surface area from 33 to 5 m^2/g (Figure 3b), which correlated with both the higher density of the aerogels and the structural transition from sheet-like to lamellar morphology (Figure 1a). Increasing the $C_{A\text{-}CNC+H\text{-}POEGMA}$ from 2.5 to 4.0 wt% at 1:5 A-CNC:H-POEGMA ratio did not significantly change aerogels (Figure 3b). Here, the effect of higher density on the surface area of aerogels was compensated for by the change in their morphology. Overall, the surface area of the aerogels was in the rage from 5 to 33 m^2/g, which is lower than that of aerogels formed CNCs only.[66,67]

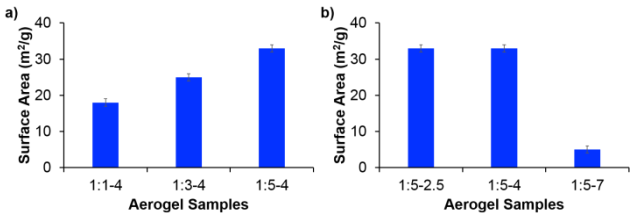

Figure 3. Surface area of (a) aerogels at a constant $C_{A\text{-}CNC+H\text{-}POEGMA}$ and varying A-CNC:H-POEGMA ratio and (b) aerogels at constant A-CNC-to-H-POEMGA ratio and varying $C_{A\text{-}CNC+H\text{-}POEGMA}$.

Small-angle X-ray scattering in aerogels. Small-angle X-ray scattering (SAXS) was used to supplement the characterization of the aerogels by SEM by providing insight into the volume-averaged aerogel structure. Figure 4 shows the SAXS data for the 1:5-4 aerogel (used as an example), as well as theoretical simulations of 2D SAXS patterns. Other 2D SAXS patterns - for fibrillar, columnar and lamellar aerogels - are given in Figure S5. The SAXS measurements were performed with the X-ray beam irradiating the aerogel in the Z- or XY-directions (corre-

sponding to the right panels in Figure 4a and b, respectively). In the case of irradiation in the Z-direction (Figure 4a, right panel), the experimental 2D pattern was isotropic (circular), while irradiation in the XY-direction yielded the anisotropic (ellipsoidal) 2D pattern (Figure 4b, right panel). These results suggested that scattering objects within the aerogel were preferentially aligned in the Z-direction but not within the XY-plane.

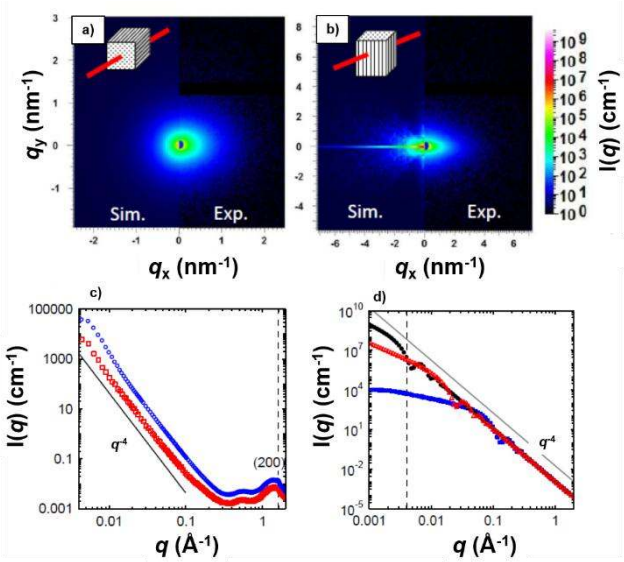

Figure 4. (a, right) Experimental 2D SAXS pattern from irradiating the 1:5-4 aerogel in the Z-direction. (a, left) Simulated 2D scattering pattern for an isotropic distribution of discs. (b, right) Experimental 2D SAXS pattern from irradiating the 1:5-4 aerogel in the XY-direction. (b, left) Simulated 2D scattering pattern for discs preferentially aligned in the Z-direction. (c) 1D radial-averaged SAXS plots of the 1:5-4 aerogel irradiated in the Z- (blue) and XY- (red) directions. A line with q^{-4} scaling is also shown as a visual aid. (d) Theoretical 1D radial-averaged SAXS plots for small cylinders (blue squares) with a radius of 3 nm (± 10 %) and a length of 150 nm; large cylinders (red triangles) with a radius of 65 nm (± 10 %) and a length of 50 µm; and discs (black dots) with a radius of 5 µm and a diameter of 260 nm (± 10 %). The dotted line marks the lower limit of the experimentally reachable q range.

Theoretical 2D SAXS patterns were simulated to determine the length scale of the aligned scattering objects. Figure 4a and b (both left panels) show the simulated patterns for model discs preferentially aligned in the Z-direction and discs with random spatial orientation, respectively. The dimensions of these discs - a radius of 5 µm and thickness of 260 nm (± 10 % - were chosen to be comparable to those of mesostructured fibrils, columnar walls, and lamellae shown in the SEM images (Figure 1a). Figure 4a (left panel) shows the simulated 2D SAXS pattern for the discs distributed isotopically. The pattern was similar to the experimental pattern (Figure 4a, right), which suggested that the mesostructures are the source of scattering and that they are not aligned in the XY-plane. Figure 4b (left panel) shows the simulated ellipsoidal 2D SAXS pattern for the discs preferentially aligned in Z-direction with a separation distance between the discs of 10 µm. The pattern was similar to the experimental pattern (Figure 4b, right), implying that the experimental scattering pattern likely originated from the scattering of mesostructures aligned in the Z-direction. In addition, the 1D radial-averaged plots for the 2D scattering patterns of 1:5-4 (Figure 4c) showed a q^{-4} scaling for q < 0.2 Å^{-1}, which implied that the scattering data were in the Porod region[68] and the scattering was dominated by objects with a size >100 nm. Thus, we conclude that the mesostructures were responsible for the main scattering contribution.

While the A-CNC components of the aerogel could be aligned by shear forces imposed by the growing ice front during uni-directional freezing, as previously suggested for freeze-cast CNC aerogels;[69] it is difficult to prove such an alignment by low-angle SAXS measurements. This is because the scattering of small cylinder-like objects such as CNCs is concealed by the scattering from larger mesoscopic fibrils, columnar walls, and lamellae. To demonstrate this effect, we showed in Figure 4d the theoretical 1D radial-averaged scattering plots for small cylinders with diameters < 10 nm (similar to A-CNCs) and for large cylinders and discs with diameters > 100 nm (similar to mesostructures in SEM images in Figure 1a). These plots show that in the low q range, scattering contributions from the small cylinders are concealed by the contribution of large structures, if both are to be present in the same sample.

Although the SAXS data at low experimental q ranges could not provide insight into the alignment of the A-CNCs in the aerogel, the scattering patterns at high q values were sensitive to the crystalline cores of A-CNCs and could reveal their alignment. The 1D radial-averaged SAXS plots for 1:5-4 aerogel irradiated in the Z- and XY-directions (Figure 4c) both show a peak at 1.6 Å^{-1} and a broad shoulder at ~0.5 Å^{-1}, attributable to the (200) and (110) reflections, respectively, from the cellulose crystal planes.[66] If the A-CNCs were aligned in the Z-direction, well-defined spot- or arc-like Bragg reflections would be expected at these q values. The 2D SAXS patterns, for the 1:5-4 aerogel irradiated in the XY- and Z-directions, show Debye-Scherrer rings (Figure S6), as opposed to spot-like Bragg reflections or defined arcs, which suggested that there is no preferential orientation of the A-CNCs in neither the Z-direction, nor in the XY-plane.

Swelling behavior of anisotropic hydrogels. The key advantage of our material is that upon aerogel rehydration, chemical cross-linking between A-CNCs and H-POEGMA constituents prevents the disintegration of the aerogel, unlike with hemiacetal crosslinked CNC hydrogels which would readily dissolve in water.[35] In addition, chemical cross-linking of the aerogel can preserve its anisotropy upon swelling.

All the aerogels examined in the present work did not disintegrate when exposed to water for the time interval up to 93 h, while Equilibrium swelling was achieved within 24 h (Figure S3, Supporting Information).

A coordinate system was used to characterize anisotropy in aerogel swelling (and mechanical properties of the hydrogels described in the following section). In Figure 5a, the Z- and XY-directions refer to the direction parallel to and perpendicular to the direction of ice growth, respectively. The anisotropic degrees of swelling of the aerogels are shown in Figures 5b and c. At $C_{A\text{-}CNC+H\text{-}POEGMA}$= 4 wt%, a higher equilibrium swelling was achieved at a higher fraction of the hydrophilic H-POEGMA (Figure 5b), in agreement with earlier reports for isotropic A-CNC-H-POEGMA hydrogels.[53]

In addition, increasing $C_{A\text{-}CNC+H\text{-}POEGMA}$ led to stronger swelling, which was attributed to both the increased osmotic pressure governing swelling in more concentrated hydrogels and a larger amount of H-POEGMA in the sample. The structural anisotropy of the aerogel led to a higher degree of swelling in the XY-direction than in the Z-direction (Student's t-test, $p < 0.05$ except for samples 1:3-4 and 1:5-7). Swelling in the Z-direction was mostly driven by the H-POEGMA component, whereas swelling in the XY-direction occurred also due to filling of the anisotropic pores with water and the resulting increase in pore size.

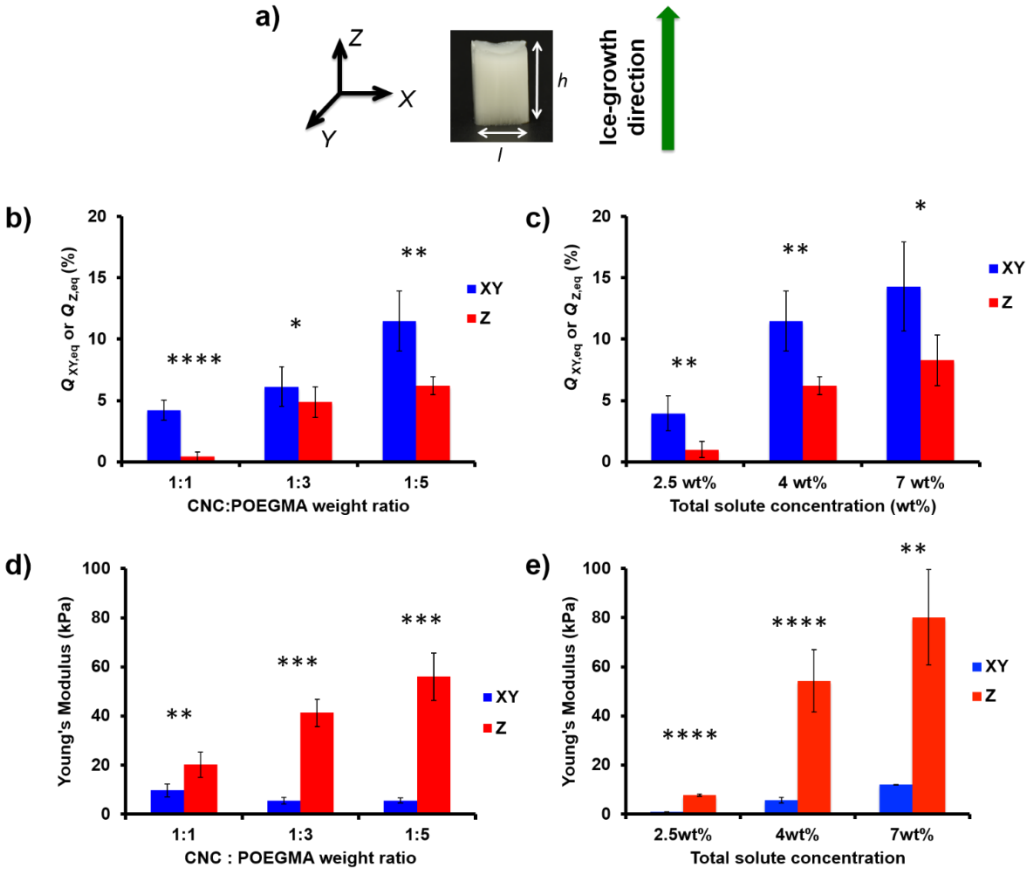

Figure 5. (a) Coordinate system used for swelling and compression tests. (b, c) Degree of swelling in the XY ($Q_{XY,eq}$) and Z ($Q_{Z,eq}$) directions of aerogels cast from suspensions at varying CNC:POEGMA weight ratio and $C_{A\text{-}CNC+H\text{-}POEGMA}$=4 wt% (b) and varying $C_{A\text{-}CNC+H\text{-}POEGMA}$ and CNC:POEGMA weight ratio of 1:5 (c). (d, e) Young's moduli of hydrogels prepared at varying CNC:POEGMA weight ratio and $C_{A\text{-}CNC+H\text{-}POEGMA}$=4 wt% (d) and varying $C_{A\text{-}CNC+H\text{-}POEGMA}$ and CNC:POEGMA weight ratio of 1:5 (e). *p >0.05, ** p <0.05, *** p <0.01, **** p <0.001, Student's t-test. The error bars represent one standard deviation. Blue and red colored bars correspond to the XY-plane and Z-directions, respectively.

Mechanical properties of anisotropic hydrogels. To characterize the mechanical integrity and direction-dependent Young's moduli of the anisotropic hydrogels (important for potential tissue engineering applications[70]), compression tests were performed on swollen hydrogels in the XY-direction (up to 50 % strain) and the Z-direction (up to 10 % strain). Supporting Information shows the videos of hydrogel compression. All hydrogels exhibited 100% shape recovery in both XY- and Z-directions after 50 compression-decompression cycles at a strain rate of 3 % of the original hydrogel dimension per second. Representative stress-strain curves for sample 1:5-4 are shown in Figure 6a (Figure S4 shows the stress-strain curves for other hydrogels). The direction-specific Young's moduli of the hydrogels are shown in Figure 5d and e. The Young's modulus in the Z-direction (E_z) was

higher than that in the XY-direction (E_{xy}) in each sample tested, consistent with the anisotropic hydrogel structures. Compression in the Z-direction led to buckling of the hydrogel fibrillar, columnar and lamellar mesostructures. In the XY-direction, at low strain, compression led to the collapse of the hydrogel pores, while at higher strain, the composite material within the hydrogel walls/fibrils was compressed. The anisotropy in hydrogel compression was less pronounced in fibrillar hydrogels. The CNC-to-POEGMA weight ratio did not have a significant

effect on hydrogel weakening upon cyclic loading (Figure S4), however as the $C_{A\text{-}CNC+H\text{-}POEGMA}$ was increased from 2.5 to 7 wt%, hydrogels exhibited fatigue over 50 compression cycles, which was attributed to the irreversible deformation of the lamellar structures (delamination).

The direction-dependent Young's moduli of anisotropic hydrogels correlated with their compositions and underlying morphologies. As shown in Figure 6b and 5d, at $C_{A\text{-}CNC+H\text{-}POEGMA}$ = 4 wt%, at lower A-CNC:H-to-POEGMA weight ratios (a higher fraction of POEGMA in the hydrogel), E_{xy} changed weakly, whele E_z strongly increased. The latter trend was counter-intuitive, since the fraction of rigid CNCs in the system reduced. We attribute this effect to the need in a higher fraction of POEGMA in the hydrogel to achieve the highest degree of chemical cross-linking between A-CNCs and H-POEGMA.

In contrast, at the A-CNC-to-H-POEGMA weight ratio of 1:5, increasing the $C_{A\text{-}CNC+H\text{-}POEGMA}$ from 2.5 to 7% led to an increase in both E_{xy} and E_z (Figure 6d and 5e). We ascribe the increase in Young's moduli in both directions to the increase in the total density of the hydrogel at a higher precursor concentration. In addition, a transition from a sheet-like structure (for 1:5-2.5 hydrogels) to a lamellar morphology (for 1:5-7

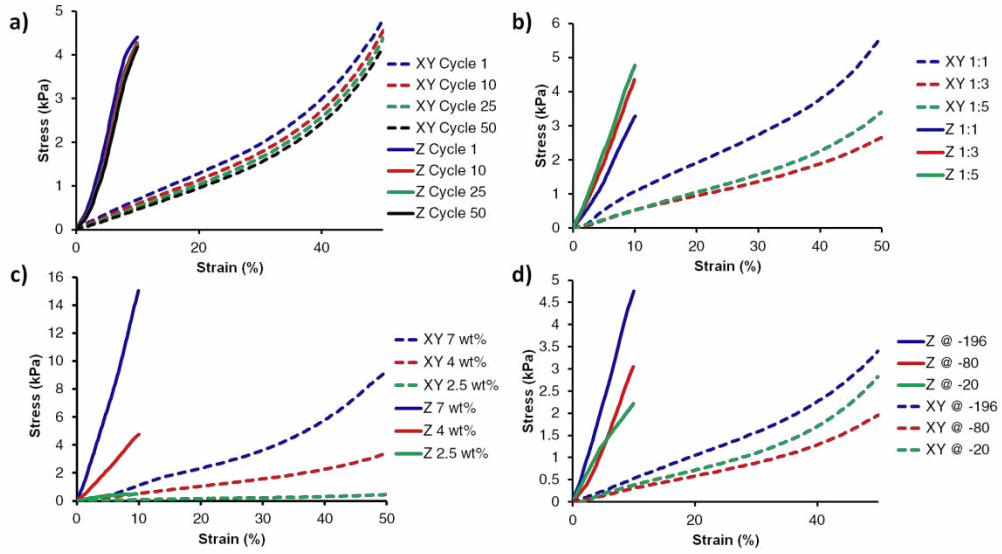

Figure 6. Mechanical properties of anisotropic hydrogels. (a) Stress-strain curves for a representative hydrogel sample (1:5-4) over 50 compression cycles. (b) The first compression cycle for hydrogels cast from suspensions prepared at varying A-CNC:H-POEGMA ratios and $C_{A\text{-}CNC+H\text{-}POEGMA}$ = 4 wt%. (c) The first compression cycle for hydrogels cast from suspensions prepared at varying $C_{A\text{-}CNC+H\text{-}POEGMA}$ and A-CNC:H-POEGMA ratio of 1:5. (d) The first compression cycle for 1:5-4 hydrogels freeze-cast at -196, -80 and -20 °C. All samples were subjected to a pre-compression and then strained for 50 compression cycles. Pre-compressions were performed at 10% and 50% strains for Z- and XY-directions, respectively.

hydrogels) resulted in the increase in the Young's moduli.

Similarly, decreasing the freeze-cast temperature yielded hydrogels with higher E_{xy} and E_z values (Figure 6d). As the freeze-cast temperature decreased, the ice front velocity increased,[71] which resulted in a tighter packing of the the CNC/POEGMA mixture excluded from the ice growing front. These tightly packed structures resulted in stiffer hydrogels.

Thus we conclude that structurally and mechanically anisotropic precursor aerogels and resulting composite hydrogels with a high structural integrity can be formed by freeze-casting a dispersion of A-CNCs and H-POEGMA. By varying the precursor composition, and/or the freeze-cast temperature, the morphology and the direction-dependent moduli of the hydrogels can be tuned and controlled. Such control may be of particular interest for mimicking biological tissues that exhibit analogous directional mechanics due to their internal orientation.

CONCLUSION

Aerogels and hydrogels of A-CNCs and H-POEGMA have been produced in a single freeze-casting/cross-linking procedure. Chemical cross-linking between A-CNCs and H-POEGMA resulted in mechanically stable hydrogels, with A-CNC component contributing to improved dimensional stability, although without structural alignment. The lamellar, columnar, and fibrillar morphologies of the material were realized by varying the total amount of A-CNCs and H-POEGMA in the precursor dispersion and the weight ratio between these constituents. The composition and morphology of the material determined anisotropic swelling and mechanical properties of the composite hydrogels. The structural integrity of the hydrogels and the capability to control their direction-dependent swelling and mechanical properties suggest that these materials may function as effective biomimetic scaffolds for tissue engineering of oriented tissues.

ASSOCIATED CONTENT

Atomic force microscopy imaging of aldehyde-modified CNCs. Setup for freeze-casting of samples at -80 to -20 °C. Kinetics of hydrogel swelling. Stress-strain curves for all samples. SAXS 2D scattering patterns.

This material is available free of charge via the Internet at http://pubs.acs.org.

AUTHOR INFORMATION

Corresponding Author

* Corresponding authors:
E. Kumacheva (ekumache@chem.utoronto.ca)
E. D. Cranston (ecranst@mcmaster.ca)
T. Hoare (hoaretr@mcmaster.ca)

Author Contributions

The manuscript was written through contributions of all authors. All authors have given approval to the final version of the manuscript.
‡These authors contributed equally.

Funding Sources

Funding for the research presented in this manuscript was con
tributed by NSERC Canada (Discovery grants RGPIN 356489, 356609 and 402329) and the NSERC CREATE IDEM program (grant 398058).

ACKNOWLEDGMENT

M. C. and K. D. acknowledge support from NSERC and NSERC CREATE Program. EK thank Canada Research Chair support. The authors also thank H. Marway for CNC AFM imaging.

ABBREVIATIONS

CNC, cellulose nanocrystal; POEGMA, poly(oligo ethylene glycol methacrylate); OEGMA500, oligo(ethylene glycol) methyl ether methacrylate; M(EO)2MA, di(ethylene glycol) methyl ether methacrylate; AA, acrylic acid; AIBMe, 2,2-azobisisobutyric acid dimethyl ester; ADH, adipic acid dihydrazide; EDC, *N*'-ethyl-*N*-(3-dimethylaminopropyl)-carbodiimide; TGA, thioglycolic acid; DIW, deionized water; CHES, *N*-cyclohexyl-2-aminoethanesulfonic acid; A-CNC, aldehyde-functionalized CNC; H-POEGMA, hydrazide-functionlized POEGMA; TEM, transmission electron microscopy; SEM, scanning electron microscopy; *E*, Young's modulus; BET, Brunauer-Emmet-Teller; SAXS, small-angle X-ray scattering.

REFERENCES

(1) Hoare, T. R.; Kohane, D. S. Hydrogels in Drug Delivery: Progress and Challenges. *Polymer (Guildf).* **2008**, *49*, 1993–2007.

(2) Hoffman, A. S. Hydrogels for Biomedical Applications. *Adv. Drug Deliv. Rev.* **2002**, *54*, 3–12.

(3) Khademhosseini, A.; Vacanti, J. P.; Langer, R. Progress in Tissue Engineering. *Sci. Am.* **2009**, *300*, 64–71.

(4) Kim, J. J.; Park, K. Smart Hydrogels for Bioseparation. *Bioseparation* **1999**, *7*, 177–184.

(5) Jing, G.; Wang, L.; Yu, H.; Amer, W. a.; Zhang, L. Recent Progress on Study of Hybrid Hydrogels for Water Treatment. *Colloids Surf., A* **2013**, *416*, 86–94.

(6) Haque, M. A.; Kurokawa, T.; Gong, J. P. Anisotropic Hydrogel Based on Bilayers: Color, Strength, Toughness, and Fatigue Resistance. *Soft Matter* **2012**, *8*, 8008–8016.

(7) Walker, K. J.; Madihally, S. V. Anisotropic Temperature Sensitive Chitosan-Based Injectable Hydrogels Mimicking Cartilage Matrix. *J. Biomed. Mater. Res. Part B Appl. Biomater.* **2014**, 1146–1160.

(8) Rudisill, S. G.; DiVito, M. D.; Hubel, A.; Stein, A. In Vitro Collagen Fibril Alignment via Incorporation of Nanocrystalline Cellulose. *Acta Biomater.* **2014**, *12*, 122–128.

(9) Aubin, H.; Nichol, J. W.; Hutson, C. B.; Bae, H.; Sieminski, A. L.; Cropek, D. M.; Akhyari, P.; Khademhosseini, A. Directed 3D Cell Alignment and Elongation in Microengineered Hydrogels. *Biomaterials* **2010**, *31*, 6941–6951.

(10) Yamada, M.; Sugaya, S.; Naganuma, Y.; Seki, M.

Microfluidic Synthesis of Chemically and Physically Anisotropic Hydrogel Microfibers for Guided Cell Growth and Networking. *Soft Matter* **2012**, *8*, 3122–3130.

(11) Li, Y.; Huang, G.; Zhang, X.; Wang, L.; Du, Y.; Lu, T. J.; Xu, F. Engineering Cell Alignment in Vitro. *Biotechnol. Adv.* **2014**, *32*, 347–365.

(12) Camarero-Espinosa, S.; Rothen-Rutishauser, B.; Weder, C.; Foster, E. J. Directed Cell Growth in Multi-Zonal Scaffolds for Cartilage Tissue Engineering. *Biomaterials* **2015**, *74*, 42–52.

(13) Swan, M. C.; Bucknall, D. G.; Goodacre, T. E. E.; Czernuszka, J. T. Synthesis and Properties of a Novel Anisotropic Self-Inflating Hydrogel Tissue Expander. *Acta Biomater.* **2011**, *7*, 1126–1132.

(14) Tseng, H.; Puperi, D. S.; Kim, E. J.; Ayoub, S.; Shah, J. V; Cuchiara, M. L.; West, J. L.; Grande-Allen, K. J. Anisotropic Poly(ethylene Glycol)/polycaprolactone Hydrogel-Fiber Composites for Heart Valve Tissue Engineering. *Tissue Eng. Part A* **2014**, *20*, 2634–2645.

(15) Voge, C. M.; Kariolis, M.; MacDonald, R. A.; Stegemann, J. P. Directional Conductivity in SWNT-Collagen-Fibrin Composite Biomaterials through Strain-Induced Matrix Alignment. *J. Biomed. Mater. Res. A* **2008**, *86*, 269–277.

(16) Dvir, T.; Timko, B. P.; Brigham, M. D.; Naik, S. R.; Karajanagi, S. S.; Levy, O.; Jin, H.; Parker, K. K.; Langer, R.; Kohane, D. S. Nanowired Three-Dimensional Cardiac Patches. *Nat. Nanotechnol.* **2011**, *6*, 720–725.

(17) Ahadian, S.; Ramón-Azcón, J.; Estili, M.; Liang, X.; Ostrovidov, S.; Shiku, H.; Ramalingam, M.; Nakajima, K.; Sakka, Y.; Bae, H.; *et al.* Hybrid Hydrogels Containing Vertically Aligned Carbon Nanotubes with Anisotropic Electrical Conductivity for Muscle Myofiber Fabrication. *Sci. Rep.* **2014**, *4*, 4271.

(18) Barrow, M.; Zhang, H. Aligned Porous Stimuli-Responsive Hydrogels via Directional Freezing and Frozen {UV} Initiated Polymerization. *Soft Matter* **2013**, *9*, 2723–2729.

(19) Mao, M.; He, J.; Liu, Y.; Li, X.; Li, D. Ice-Template-Induced Silk Fibroin-Chitosan Scaffolds with Predefined Microfluidic Channels and Fully Porous Structures. *Acta Biomater.* **2012**, *8*, 2175–2184.

(20) Chen, M.; Zhu, J.; Qi, G.; He, C.; Wang, H. Anisotropic Hydrogels Fabricated with Directional Freezing and Radiation-Induced Polymerization and Crosslinking Method. *Mater. Lett.* **2012**, *89*, 104–107.

(21) Zhu, J.; Wang, J.; Liu, Q.; Liu, Y.; Wang, L.; He, C.; Wang, H. Anisotropic Tough poly(2-Hydroxyethyl Methacrylate) Hydrogels Fabricated by Directional Freezing Redox Polymerization. *J. Mater. Chem. B* **2013**, *1*, 978–986.

(22) Paz, A. C.; Soleas, J.; Poon, J. C. H.; Trieu, D.; Waddell, T. K.; McGuigan, A. P. Challenges and Opportunities for Tissue-Engineering Polarized Epithelium. *Tissue Eng. Part B. Rev.* **2014**, *20*, 56–72.

(23) Engler, A. J.; Sen, S.; Sweeney, H. L.; Discher, D. E. Matrix Elasticity Directs Stem Cell Lineage Specification. *Cell* **2006**, *126*, 677–689.

(24) He, J.; Wang, Y.; Liu, Y.; Li, D.; Jin, Z. Layer-by-Layer Micromolding of Natural Biopolymer Scaffolds with Intrinsic Microfluidic Networks. *Biofabrication* **2013**, *5*, 025002.

(25) He, J.; Mao, M.; Liu, Y.; Zhu, L.; Li, D. Bottom-up Fabrication of 3D Cell-Laden Microfluidic Constructs. *Mater. Lett.* **2013**, *90*, 93–96.

(26) Barrow, M.; Eltmimi, A.; Ahmed, A.; Myers, P.; Zhang, H. Frozen Polymerization for Aligned Porous Structures with Enhanced Mechanical Stability, Conductivity, and as Stationary Phase for HPLC. *J. Mater. Chem.* **2012**, *22*, 11615–11620.

(27) Chatelin, S.; Bernal, M.; Deffieux, T.; Papadacci, C.; Flaud, P.; Nahas, A.; Boccara, C.; Gennisson, J.-L.; Tanter, M.; Pernot, M. Anisotropic Polyvinyl Alcohol Hydrogel Phantom for Shear Wave Elastography in Fibrous Biological Soft Tissue: A Multimodality Characterization. *Phys. Med.*

Biol. **2014**, *59*, 6923–6940.

(28) Osorio-Madrazo, A.; Eder, M.; Rueggeberg, M.; Pandey, J. K.; Harrington, M. J.; Nishiyama, Y.; Putaux, J.-L.; Rochas, C.; Burgert, I. Reorientation of Cellulose Nanowhiskers in Agarose Hydrogels under Tensile Loading. *Biomacromolecules* **2012**, *13*, 850–856.

(29) Yang, W.; Furukawa, H.; Gong, J. P. Highly Extensible Double-Network Gels with Self-Assembling Anisotropic Structure. *Adv. Mater.* **2008**, *20*, 4499–4503.

(30) Zhang, S.; Greenfield, M. a; Mata, A.; Palmer, L. C.; Bitton, R.; Mantei, J. R.; Aparicio, C.; de la Cruz, M. O.; Stupp, S. I. A Self-Assembly Pathway to Aligned Monodomain Gels. *Nat. Mater.* **2010**, *9*, 594–601.

(31) Hockaday, L. A.; Kang, K. H.; Colangelo, N. W.; Cheung, P. Y. C.; Duan, B.; Malone, E.; Wu, J.; Girardi, L. N.; Bonassar, L. J.; Lipson, H.; *et al.* Rapid 3D Printing of Anatomically Accurate and Mechanically Heterogeneous Aortic Valve Hydrogel Scaffolds. *Biofabrication* **2012**, *4*, 035005.

(32) Barrow, M.; Zhang, H. Aligned Porous Stimuli-Responsive Hydrogels via Directional Freezing and Frozen UV Initiated Polymerization. *Soft Matter* **2013**, *9*, 2723–2729.

(33) Liu, H.; Nakagawa, K.; Chaudhary, D.; Asakuma, Y.; Tadé, M. O. Freeze-Dried Macroporous Foam Prepared from Chitosan/xanthan Gum/montmorillonite Nanocomposites. *Chem. Eng. Res. Des.* **2011**, *89*, 2356–2364.

(34) Yokoyama, F.; Achife, E. C.; Momoda, J.; Shimamura, K.; Monobe, K. Morphology of Optically Anisotropic Agarose Hydrogel Prepared by Directional Freezing. *Colloid Polym. Sci.* **1990**, *268*, 552–558.

(35) Köhnke, T.; Elder, T.; Theliander, H.; Ragauskas, A. J. Ice Templated and Cross-Linked Xylan/nanocrystalline Cellulose Hydrogels. *Carbohydr. Polym.* **2014**, *100*, 24–30.

(36) Wicklein, B.; Kocjan, A.; Salazar-Alvarez, G.; Carosio, F.; Camino, G.; Antonietti, M.; Bergström, L. Thermally Insulating and Fire-Retardant Lightweight Anisotropic Foams Based on Nanocellulose and Graphene Oxide. *Nat. Nanotechnol.* **2015**, *10*, 277–283.

(37) Darder, M.; Aranda, P.; Ferrer, M. L.; Gutiérrez, M. C.; del Monte, F.; Ruiz-Hitzky, E. Progress in Bionanocomposite and Bioinspired Foams. *Adv. Mater.* **2011**, *23*, 5262–5267.

(38) Deville, S. Freeze-Casting of Porous Ceramics: A Review of Current Achievements and Issues. *Adv. Eng. Mater.* **2008**, *10*, 155–169.

(39) Gutiérrez, M. C.; Ferrer, M. L.; del Monte, F. Ice-Templated Materials: Sophisticated Structures Exhibiting Enhanced Functionalities Obtained after Unidirectional Freezing and Ice-Segregation-Induced Self-Assembly †. *Chem. Mater.* **2008**, *20*, 634–648.

(40) Wu, J.; Zhao, Q.; Sun, J.; Zhou, Q. Preparation of Poly(ethylene Glycol) Aligned Porous Cryogels Using a Unidirectional Freezing Technique. *Soft Matter* **2012**, *8*, 3620–3626.

(41) Bai, H.; Polini, A.; Delattre, B.; Tomsia, A. P. Thermoresponsive Composite Hydrogels with Aligned Macroporous Structure by Ice-Templated Assembly. *Chem. Mater.* **2013**, *25*, 4551–4556.

(42) Wu, J.; Lin, Y.; Sun, J. Anisotropic Volume Change of poly(N-Isopropylacrylamide)-Based Hydrogels with an Aligned Dual-Network Microstructure. *J. Mater. Chem.* **2012**, *22*, 17449–17451.

(43) Wu, X.; Liu, Y.; Li, X.; Wen, P.; Zhang, Y.; Long, Y.; Wang, X.; Guo, Y.; Xing, F.; Gao, J. Preparation of Aligned Porous Gelatin Scaffolds by Unidirectional Freeze-Drying Method. *Acta Biomater.* **2010**, *6*, 1167–1177.

(44) Habibi, Y.; Lucia, L. a; Rojas, O. J. Cellulose Nanocrystals: Chemistry, Self-Assembly, and Applications. *Chem. Rev.* **2010**, *110*, 3479–3500.

(45) Yang, X.; Bakaic, E.; Hoare, T.; Cranston, E. D. Injectable Polysaccharide Hydrogels Reinforced with Cellulose Nanocrystals: Morphology, Rheology, Degradation, and Cytotoxicity. *Biomacromolecules* **2013**, *14*, 4447–4455.

(46) Yang, J.; Zhao, J.-J.; Xu, F.; Sun, R.-C. Revealing Strong

Nanocomposite Hydrogels Reinforced by Cellulose Nanocrystals: Insight into Morphologies and Interactions. *ACS Appl. Mater. Interfaces* **2013**, *5*, 12960–12967.

(47) Zhou, C.; Wu, Q.; Yue, Y.; Zhang, Q. Application of Rod-Shaped Cellulose Nanocrystals in Polyacrylamide Hydrogels. *J. Colloid Interface Sci.* **2011**, *353*, 116–123.

(48) Yang, J.; Zhao, J.-J.; Han, C.-R.; Duan, J.-F.; Xu, F.; Sun, R.-C. Tough Nanocomposite Hydrogels from Cellulose Nanocrystals/poly(acrylamide) Clusters: Influence of the Charge Density, Aspect Ratio and Surface Coating with PEG. *Cellulose* **2013**, *21*, 541–551.

(49) Yang, J.; Han, C.-R.; Zhang, X.-M.; Xu, F.; Sun, R.-C. Cellulose Nanocrystals Mechanical Reinforcement in Composite Hydrogels with Multiple Cross-Links: Correlations between Dissipation Properties and Deformation Mechanisms. *Macromolecules* **2014**, *47*, 4077–4086.

(50) Siham Atifi, Shunxing Su, W. Y. H. Mechanically Tunable Nanocomposite Hydrogels Based on Functionalized Cellulose Nanocrystals. *Nord. Pulp Pap. Res. J.* **2014**, *29*, 95–104.

(51) Hebeish, A.; Farag, S.; Sharaf, S.; Shaheen, T. I. Thermal Responsive Hydrogels Based on Semi Interpenetrating Network of poly(NIPAm) and Cellulose Nanowhiskers. *Carbohydr. Polym.* **2014**, *102*, 159–166.

(52) Yang, J.; Han, C.; Xu, F.; Sun, R. Simple Approach to Reinforce Hydrogels with Cellulose Nanocrystals. *Nanoscale* **2014**, *6*, 5934–5943.

(53) De France, K. J.; Chan, K. J. W.; Cranston, E. D.; Hoare, T. Enhanced Mechanical Properties in Cellulose Nanocrystal-Poly(oligo Ethylene Glycol Methacrylate) Injectable Nanocomposite Hydrogels through Control of Physical and Chemical Cross-Linking. *Biomacromolecules* **2016**, *17*, 649–660.

(54) Chiang, Y.; Kresge, A. J. Kinetics of Hydrolysis of Acetaldehyde Ethyl Hemiacetal in Aqueous Solution. *J. Org. Chem.* **1985**, *50*, 5038–5040.

(55) Smeets, N. M. B.; Bakaic, E.; Patenaude, M.; Hoare, T. Injectable Poly(oligoethylene Glycol Methacrylate)-Based Hydrogels with Tunable Phase Transition Behaviours: Physicochemical and Biological Responses. *Acta Biomater.* **2014**, *10*, 4143–4155.

(56) Moon, R. J.; Martini, A.; Nairn, J.; Simonsen, J.; Youngblood, J. Cellulose Nanomaterials Review: Structure, Properties and Nanocomposites. *Chem. Soc. Rev.* **2011**, *40*, 3941–3994.

(57) Eichhorn, S. J. Cellulose Nanowhiskers: Promising Materials for Advanced Applications. *Soft Matter* **2011**, *7*, 303–315.

(58) Azizi Samir, M. A. S.; Alloin, F.; Dufresne, A. Review of Recent Research into Cellulosic Whiskers, Their Properties and Their Application in Nanocomposite Field. *Biomacromolecules* **2005**, *6*, 612–626.

(59) Lutz, J.-F. Polymerization of Oligo(ethylene Glycol) (meth)acrylates: Toward New Generations of Smart Biocompatible Materials. *J. Polym. Sci. Part A Polym. Chem.* **2008**, *46*, 3459–3470.

(60) Smeets, N. M. B.; Bakaic, E.; Patenaude, M.; Hoare, T. Injectable and Tunable Poly(ethylene Glycol) Analogue Hydrogels Based on Poly(oligoethylene Glycol Methacrylate). *Chem. Commun.* **2014**, *50*, 3306–3309.

(61) Beck-candanedo, S.; Roman, M.; Gray, D. G. Effect of Reaction Conditions on the Properties and Behavior of Wood Cellulose Nanocrystal Suspensions. *Biomacromolecules* **2005**, *6*, 1048–1054.

(62) Beck, S.; Méthot, M.; Bouchard, J. General Procedure for Determining Cellulose Nanocrystal Sulfate Half-Ester Content by Conductometric Titration. *Cellulose* **2014**, *22*, 101–116.

(63) Sun, B.; Hou, Q.; Liu, Z.; Ni, Y. Sodium Periodate Oxidation of Cellulose Nanocrystal and Its Application as a Paper Wet Strength Additive. *Cellulose* **2015**, *22*, 1135–1146.

(64) Brunauer, S.; Emmett, P. H.; Teller, E. Adsorption of Gases in Multimolecular Layers. *J. Am. Chem. Soc.* **1938**, *60*, 309–

319.

(65) Förster, S.; Fischer, S.; Zielske, K.; Schellbach, C.; Sztucki, M.; Lindner, P.; Perlich, J. Calculation of Scattering-Patterns of Ordered Nano- and Mesoscale Materials. *Adv. Colloid Interface Sci.* **2011**, *163*, 53–83.

(66) Kumar, A.; Negi, Y. S.; Choudhary, V.; Bhardwaj, N. K. Characterization of Cellulose Nanocrystals Produced by Acid-Hydrolysis from Sugarcane Bagasse as Agro-Waste. *J. Mater. Phys. Chem.* **2014**, *2*, 1–8.

(67) Heath, L.; Thielemans, W. Cellulose Nanowhisker Aerogels. *Green Chem.* **2010**, *12*, 1448–1453.

(68) Seeck, O. H.; Murphy, B. *X-Ray Diffraction: Modern Experimental Techniques*; Pan Stanford Publishing, 2015.

(69) Han, J.; Zhou, C.; Wu, Y.; Liu, F.; Wu, Q. Self-Assembling Behavior of Cellulose Nanoparticles during Freeze-Drying: Effect of Suspension Concentration, Particle Size, Crystal Structure, and Surface Charge. *Biomacromolecules* **2013**, *14*, 1529–1540.

(70) Tibbitt, M. W.; Rodell, C. B.; Burdick, J. A.; Anseth, K. S. Progress in Material Design for Biomedical Applications. *Proc. Natl. Acad. Sci.* **2015**, *112*, 201516247.

(71) Deville, S.; Saiz, E.; Tomsia, A. P. Ice-Templated Porous Alumina Structures. *Acta Mater.* **2007**, 55, 1965–1974.